The January 2022 eruption of Hunga Tonga-Hunga Ha'apai volcano reached the mesosphere

Simon Richard Proud[1], Andrew Prata[2], and Simeon Schmauss[3]

[1]UKRI Rutherford Appleton Laboratory
[2]University of Oxford
[3]Munich University of Applied Sciences

November 26, 2022

Abstract

Explosive volcanic eruptions can loft ash, gases and water into the stratosphere, which affects both human activities and the climate. Using geostationary satellite images of the January 2022 Hunga-Tonga volcano eruption we find that the volcanic cloud produced by this volcano reached an altitude of 57km at its highest extent. This places the cloud in the lower mesosphere and provides the first observational evidence of a volcanic eruption injecting material through the stratosphere and directly into the mesosphere. We then discuss potential implications of this injection and suggest that the altitude reached by plumes from previous eruptions, such as Pinatubo in 1991, are very likely to be underestimated.

Title: The January 2022 eruption of Hunga Tonga-Hunga Ha'apai volcano reached the mesosphere

Authors: Simon R Proud[1,2]*, Andrew T Prata[2], Simeon Schmauß[3]

Affiliations:

[1]National Centre for Earth Observation, RAL Space, STFC Rutherford Appleton Laboratory, Harwell, OX11

[2]Atmospheric, Oceanic and Planetary Physics, University of Oxford, Parks Road, Oxford, OX1 3PU

[3]Munich University of Applied Sciences, Lothstr. 34, 80335 Munich, Germany

*Corresponding author. Email: simon.proud@stfc.ac.uk

Abstract: Explosive volcanic eruptions can loft ash, gases and water into the stratosphere, which affects both human activities and the climate. Using geostationary satellite images of the January 2022 Hunga-Tonga volcano eruption we find that the volcanic cloud produced by this volcano reached an altitude of 57km at its highest extent. This places the cloud in the lower mesosphere and provides the first observational evidence of a volcanic eruption injecting material through the stratosphere and directly into the mesosphere. We then discuss potential implications of this injection and suggest that the altitude reached by plumes from previous eruptions, such as Pinatubo in 1991, are very likely to be underestimated.

One-Sentence Summary: Large volcanic eruptions often reach the stratosphere, but here we show evidence that the January 2022 eruption of Hunga-Tonga reached beyond the stratosphere and into the mesosphere.

Main Text: Large explosive volcanic eruptions are significant as they can impact climate *(1)*, disrupt aviation *(2)* and pose a numerous hazards to communities living nearby active volcanoes *(3, 4)*. The degree to which explosive volcanic eruptions affect climate is largely dependent on the volcano's latitude, the plume height, and the amount of SO2 gas that is released *(5)*. When a significant amount of SO2 is released into the stratosphere it converts to sulphate aerosols that can, in the most extreme cases, persist for several years *(6)* and when injected at low latitudes the aerosol disperses into both hemispheres *(1, 7)*. The persistent aerosol veil that is produced impacts climate due to the reflection of incoming visible radiation and absorption of near-infrared radiation *(8)*, that results in a cooling of the troposphere *(9)* and heating of the stratosphere *(10)*. Within the satellite era, there are numerous examples of volcanic plumes reaching the upper-tropopause lower-stratosphere (UTLS) *(11,12)*; however, few have been observed to reach higher than 30 km and impact the climate *(13)*. Notable examples that have been observed and quantified using satellite observations include Mt Pinatubo (Philippines) in 1991 that injected ∼20 Tg of SO2 *(14)* and reached 40 km at its highest point *(15)* and El Chich´on that released ∼7.5 Tg of SO2 into the atmosphere *(16)*, reaching 31 km *(17)*. Based on the satellite data record, in general, individual explosive volcanic eruptions are not expected to have a measurable climate impact unless >1 Tg SO2 is released into the stratosphere *(13)*.

The Hunga Tonga-Hunga Haapai volcano (20.536°S, 175.382°W) is an underwater caldera volcano located approximately 70 km North-northwest of Tonga's capital, Nukualofa. Recent Surtseyan-style eruptive activity was observed in 2009, 2014-15 and from 20 December 2021 *(18)*. In the lead up to the 15 January 2022 eruption, described below, a large hreatomagmatic eruption, similar to the December 2019 eruption of Anak Krakatau, Indonesia *(19)*, was observed on 13 January in geostationary satellite data. The volcanological setting of Hunga Tonga-Hunga Haapai is very different compared to the Pinatubo and El Chich´on volcanoes due to the abundance of seawater available for magma interaction. Initial estimates of the total mass of SO2 released by the 15 January eruption from hyperspectral sounders and ultraviolet instruments was 0.2-0.4 Tg SO2 *(20)*. This amount of SO2 is low given the magnitude of this eruption and suggests that large amounts of SO2 may have been scavenged through wet deposition *(19, 21)*.

On 15th January 2022 at approximately 4am UTC (5pm local time) the Hunga-Tonga volcano violently erupted, producing the large volcanic cloud, shown in Figure 1. A second, smaller, eruption occurred at 8am UTC with no further large eruptions occurring thereafter. This eruption was one of the most powerful in recent years, triggering a tsunami that was felt across the Pacific and atmospheric waves that circled the Earth multiple times, which were seen as fluctuations in global pressure sensor readings for several days. The volcano's location is well-covered by satellite sensors, with three geostationary weather satellite platforms providing imagery of the area at visible and infrared wavelengths every ten minutes, summarized in supplementary Table 1, and at approximately 07:05 UTC the National Oceanic and Atmospheric Administration (NOAA) enabled a fast-scanning mesoscale sector over the volcano, producing imagery every minute.

Typically, the altitude of a volcanic plume is estimated from its cloud top temperature measured by satellite compared to a vertical profile of temperature from radiosonde measurements or weather model output such as that produced by the European Centre for Medium-Range Weather Forecasts (ECMWF) *(22)*. This technique makes use the relationship of decreasing atmospheric temperature - and hence cloud temperature for a cloud in thermodynamic equilibrium with its surroundings - with altitude in the troposphere *(23)*. However, for large volcanic eruptions the cloud penetrates the tropopause and enters the stratosphere where temperature increases with

altitude, thus rendering temperature-based techniques inaccurate: In such cases the plume in the stratosphere will initially be cooler than the ambient air but will warm as the plume enters thermodynamic equilibrium with its surroundings, which presents several possible altitude solutions for a single cloud temperature. This is further complicated as the eruption itself is likely to affect local vertical temperature profiles. In this report, we make use of the multiple satellite sensors that viewed the eruption from very different viewing geometries to compute plume altitude based on the parallax effect, which does not suffer from the limitations described above, and find that the Hunga-Tonga eruption not only penetrated the stratosphere but reached the lower mesosphere.

When a satellite views a high-altitude cloud, the cloud location within the satellite image will be incorrect due to a parallax shift whose magnitude depends on the viewing angle between satellite and cloud and upon the cloud altitude. If two or more satellites view a cloud from differing locations, then its actual position and altitude are found by iteratively adjusting estimated cloud altitude to minimize the difference in parallax corrected position between satellites *(24)*. We have previously used this approach to successfully estimate the altitude and trajectory of the Chelyabinsk Meteor *(25)*, demonstrating that the technique is appropriate for high altitude clouds. Here, we apply the approach to a series of manually selected cloud positions observed by Himawari-8 and GEO-KOMPSAT-2A (GK-2A) to the West of the Eruption and GOES-17 to the East across images taken between 04:16 UTC and 06:36 UTC, after which the sun set. In addition, we perform a more detailed analysis of the 04:36 UTC imagery from Himawari-8 and GK-2A to map variations in altitude across the plume, which is shown in Figure 2. Because these methods rely on manual point selection and analysis, they cannot map altitude across the whole plume. To gain a broad perspective of plume altitude we therefore also applied a stereoscopic vision tool to estimate altitude, which is less accurate but can provide spatial information, and the standard temperature-based retrieval described above. The results of all three techniques are shown in Fig 3. Further information on the methods used here, including tables of parallax-retrieved altitudes, are given in the supplementary materials.

Altitude retrievals from the early phase of the eruption show a rapidly ascending cloud layer, reaching 25km approximately 15 minutes after the eruption begun and 40km, in the upper stratosphere, after 25 minutes. By 04:36, half an hour after the eruption began, a dome of cloud, approximately 90km in diameter, is visible that extends from 34km up to 57km altitude (approx. 0.3hPa in the ECMWF analysis), which is 13km above the stratopause (1.5hPa) – well within the mesosphere. We estimate the uncertainty on this altitude to be less than 1.5km. Surrounding this dome is a donut-shaped structure with altitudes peaking at 41km (2.2hPa) and a secondary layer just above the ECMWF tropopause at 17.5km (91hPa). A schematic of the eruption at this point is shown in Fig 4. Ten minutes later, the dome collapsed to leave the expanding donut cloud, although haziness visible in the central region above the volcano indicates that high altitude aerosol such as sulphates or ash is likely to be present. This haze is too optically thin, however, to support altitude retrieval. By 04:56 UTC the eruption produced a new vertical column of cloud stretching from the surface to the mesosphere, including two tendrils that reach 58km (0.28hPa). These tendrils cast a shadow onto the main volcanic umbrella, now at 35km altitude, and calculation tendril altitude from the shadow length gives an altitude of 57.5km, closely matching the parallax-derived altitude. Thereafter, as shown in Fig 3, plume altitude decreases and no further mesospheric intrusions were detected. Analysis of the infrared imagery shows two plumes over the next twelve hours: One, moving South-West in the prevailing winds at 30-35km altitude and one moving East at the tropopause.

The influence of volcanoes on the mesosphere is unclear. Previous eruptions into the stratosphere have indirectly affected the mesosphere through the upward ascent transport of volcanic aerosols after an eruption *(26)*, although the chemical processes acting on mesospheric volcanic aerosols are the subject of debate *(27)*. Vertical propagation of gravity waves from volcanoes can affect the mesospheric temperature *(28)* while the aerosols and water vapor injected to high altitude by the Krakatoa eruption may have been responsible for subsequent apparent increases in mesospheric cloud. However, there is no agreement as some volcanic eruptions but not others are associated with mesospheric cloud increases *(29)*. Our observations of the Hunga-Tonga plume provide the first direct evidence that volcanic eruptions can inject material into the mesosphere and will enable more detailed analysis of mesospheric chemistry and transport. However, our work also raises questions - what mechanisms contributed to this eruption reaching such high altitude and yet appears to have released comparatively little SO2? What is the hazy substance visible atop the highest clouds and how long will it persist in the mesosphere? In addition, we show that the mesospheric altitudes achieved by this plume were only visible in satellite images taken at two times (04:30 and 04:50 UTC), highlighting the importance of frequent - every ten minutes in this case - satellite observations. Previous eruptions, such as Pinatubo, were observed much less frequently by satellite, making it very likely that the time of peak altitude associated with their volcanic plumes was not observed and that we are likely to be underestimating plume altitude by a significant amount.

References and Notes

1. Robock, Volcanic eruptions and climate 38, 191–219.

2. T. J. Casadevall, Volcanic ash and aviation safety: proceedings of the first international symposium on volcanic ash and aviation safety, no. 2047 (US Government Printing Office, 1994).

3. S. C. Loughlin, et al., Global volcanic hazards and risk (Cambridge University Press).

4. T. M. Wilson, S. Jenkins, C. Stewart, Volcanic Hazards, Risks and Disasters (Elsevier, 2015), pp. 47–86.

5. C. Schnetzler, G. Bluth, A. Krueger, L. Walter, A proposed volcanic sulfur dioxide index (vsi), Journal of Geophysical Research: Solid Earth 102, 20087–20091 (1997).

6. S. Kremser, et al., Stratospheric aerosol-observations, processes, and impact on climate: Stratospheric aerosol 54, 278–335.

7. J. Hansen, A. Lacis, R. Ruedy, M. Sato, Potential climate impact of mount pinatubo eruption, Geophysical Research Letters 19, 215–218 (1992).

8. G. L. Stenchikov, et al., Radiative forcing from the 1991 mount pinatubo volcanic eruption 103, 13837–13857.

9. E. G. Dutton, J. R. Christy, Solar radiative forcing at selected locations and evidence for global lower tropospheric cooling following the eruptions of el chich´on and pinatubo 19, 2313–2316.

10. K. Labitzke, M. P. McCormick, Stratospheric temperature increases due to Pinatubo aerosols 19, 207–210.

11. G. L. Stenchikov, et al., Radiative forcing from the 1991 mount pinatubo volcanic eruption, Journal of Geophysical Research: Atmospheres 103, 13837–13857 (1998).

12. A. Bernard, W. I. Rose, The injection of sulfuric acid aerosols in the stratosphere by the el chich´on volcano and its related hazards to the international air traffic, Natural Hazards 3, 59–67 (1990).

13. S. Carn, L. Clarisse, A. Prata, Multi-decadal satellite measurements of global volcanic degassing 311, 99–134.

14. S. Guo, G. J. Bluth, W. I. Rose, I. M. Watson, A. Prata, Re-evaluation of so2 release of the 15 June 1991 Pinatubo eruption using ultraviolet and infrared satellite sensors, Geochemistry, Geophysics, Geosystems (2004)

15. R. E. Holasek, S. Self, A. W. Woods, Satellite observations and interpretation of the 1991 mount pinatubo eruption plumes 101, 27635–27655.

16. A. Krueger, N. Krotkov, S. Carn, El chichon: The genesis of volcanic sulfur dioxide monitoring from space 175, 408–414.

17. M. Matson, The 1982 el chich´on volcano eruptions — a satellite perspective 23, 1–10.

18. M. Brenna, et al., Post-caldera volcanism reveals shallow priming of an intra-ocean arc andesitic caldera: Hunga volcano, Tonga, SW pacific.

19. A. T. Prata, et al., Anak krakatau triggers volcanic freezer in the upper troposphere

20.   S. K. e. Sennert, Report on hunga tonga-hunga ha'apai (tonga).

21.   W. I. Rose, et al., Ice in the 1994 rabaul eruption cloud: implications for volcano hazard and atmospheric effects 375, 477–479.

22.   R. G. Owens, T. Hewson, Ecmwf forecast user guide (2018).

23.   M. Stengel, et al., Cloud property datasets retrieved from avhrr, modis, aatsr and meris in the framework of the cloud cci project, earth syst. sci. data, 9, 881–904 (2017).

24.   L. Merucci, K. Zakˇsek, E. Carboni, S. Corradini, Stereoscopic estimation of volcanic ash cloud-top height from two geostationary satellites, Remote Sensing 8, 206 (2016).

25.   S. Proud, Reconstructing the orbit of the chelyabinsk meteor using satellite observations, Geophysical research letters 40, 3351–3355 (2013).

26.   M. J. Mills, O. B. Toon, G. E. Thomas, Mesospheric sulfate aerosol layer, Journal of Geophysical Research: Atmospheres 110 (2005).

27.   C. George, et al., Emerging areas in atmospheric photochemistry, Atmospheric and aerosol chemistry pp. 1–53 (2012).

28.   C. von Savigny, et al., The research unit volimpact: Revisiting the volcanic impact on atmosphere and climate–preparations for the next big volcanic eruption, Meteorologische Zeitschrift pp. 3–18 (2020).

29.   C. Bertolin, F. Domınguez-Castro, The earliest datable noctilucent cloud observation (parma, italy, ad 1840), The Holocene 30, 682–690 (2020).

30.   M. Raspaud, et al., Pytroll: An open-source, community-driven python framework to process earth observation satellite data, Bulletin of the American Meteorological Society 99, 1329–1336 (2018).

31.   L. Lastilla, V. Belloni, R. Ravanelli, M. Crespi, Dsm generation from single and cross-sensor multi-view satellite images using the new agisoft metashape: The case studies oftrento and matera (italy), Remote Sensing 13, 593 (2021)

32.   T. J. Schmit, et al., A closer look at the ABI on the GOES-R series, Bulletin of the American Meteorological Society 98, 681–698 (2017).

33.   K. Bessho, et al., An introduction to himawari-8/9—japan's new-generation geostationary meteorological satellites, Journal of the Meteorological Society of Japan. Ser. II94, 151–183 (2016).

34.   D. Kim, M. Gu, T.-H. Oh, E.-K. Kim, H.-J. Yang, Introduction of the advanced meteorological imager of geo-kompsat-2a: In-orbit tests and performance validation, Remote Sensing 13, 1303 (2021).

Acknowledgments

5

10

Data Availability: GOES-16 and Himawari-8 satellite data are available through NOAA's big data program: https://www.noaa.gov/organization/information-technology/list-of-big-dataprogram-datasets

15 GK-2A data is available via KMA's open data API: https://datasvc.nmsc.kma.go.kr/

ECMWF and GFS profile data (filename TProfs.csv) and the Python code used to perform this analysis is available on GitHub: https://github.com/simonrp84/Tonga_Volcano_Code

The lists of points used for tri- and dual-satellite parallax calculations are also on the same GitHub page (filenames: Points_Dual.csv and Points_Tri.csv). The IR and stereoscopic retrieval outputs are in the Height_Out and Heightmap subdirectories respectively.

20

Supplementary Materials

Materials and Methods

Table S1

25

30

35

40
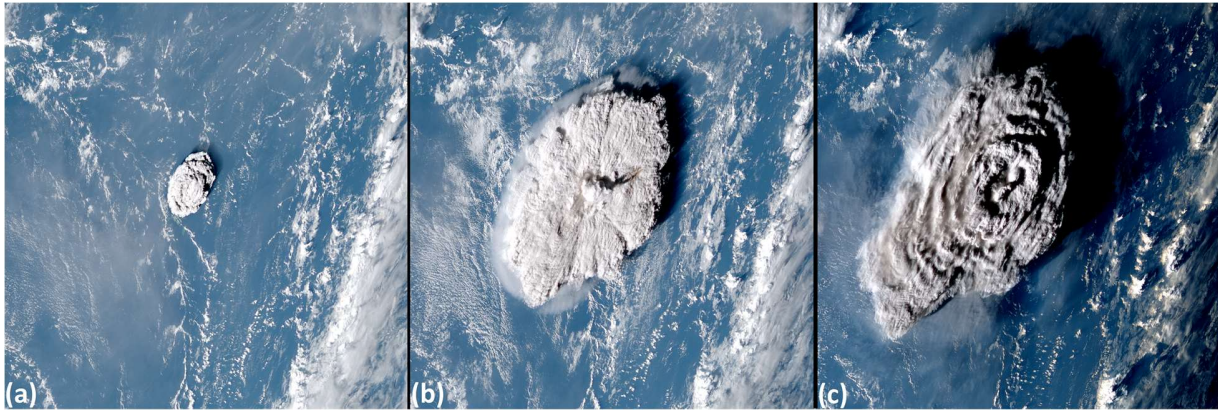
Fig. 1. The Hunga-Tonga eruption viewed from the Himawari-8 weather satellite. (a) At 04:10 UTC, approximately ten minutes after the Eruption began. (b) At 04:50 UTC after the initial dome collapsed, leaving remnants at 55-58km altitude that case a shadow (to right) onto the umbrella cloud at 34km. (c) At 05:40 UTC as the volcanic umbrella spreads South-Westwards and the sun begins to set, emphasizing the shadows that we used to calculate plume altitude and highlighting wave structure in the umbrella top.

5
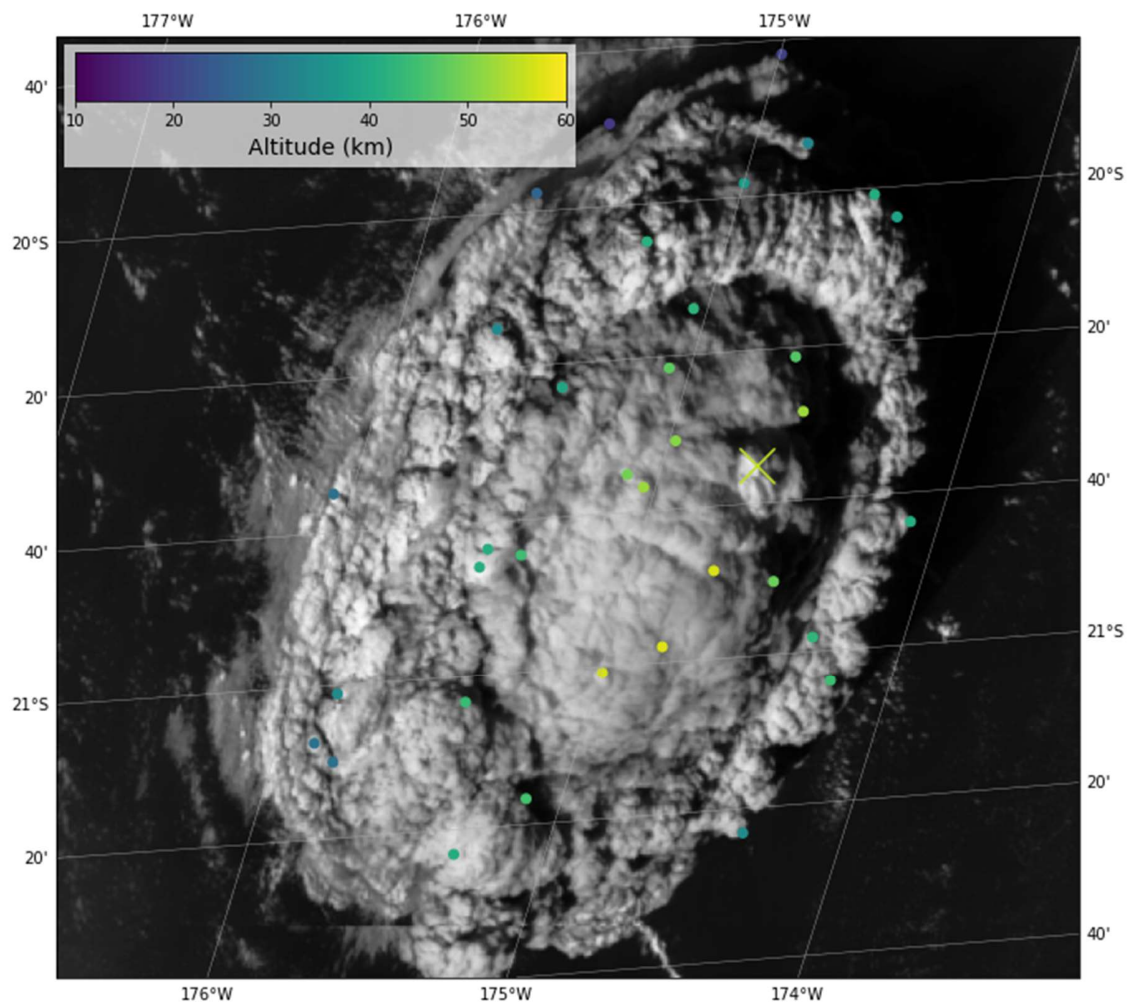
Fig 2. Parallax-based retrievals of plume cloud altitude at 04:30 UTC overlaid on Himawari-8 / AHI high resolution data for the same time frame. Coloured circles represent AHI-AMI retrievals and the two crosses denote AHI-AMI-ABI retrievals.
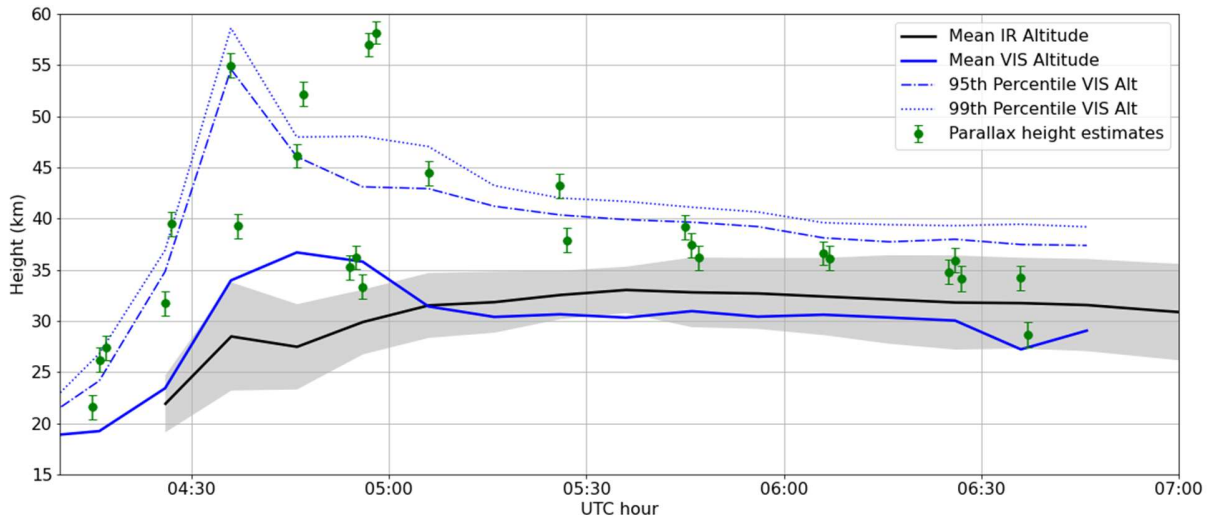
Fig 3. Temporal evolution of volcanic plume altitude derived from visible and infrared data. Infrared heights are derived from Himawari-8 brightness temperature measurements and the ECMWF temperature profile. The grey shaded area represents one standard deviation from the mean. The blue lines denote altitudes estimated via the stereoscopic method across the entire volcanic plume and the green markers are parallax heights derived from manual analysis of data from Himawari-8, GK-2A and GOES-17. Error bars show the spread of estimated altitudes due to simulated geo-location uncertainty. Due to sunset, no visible altitudes are available after 06:46 UTC.
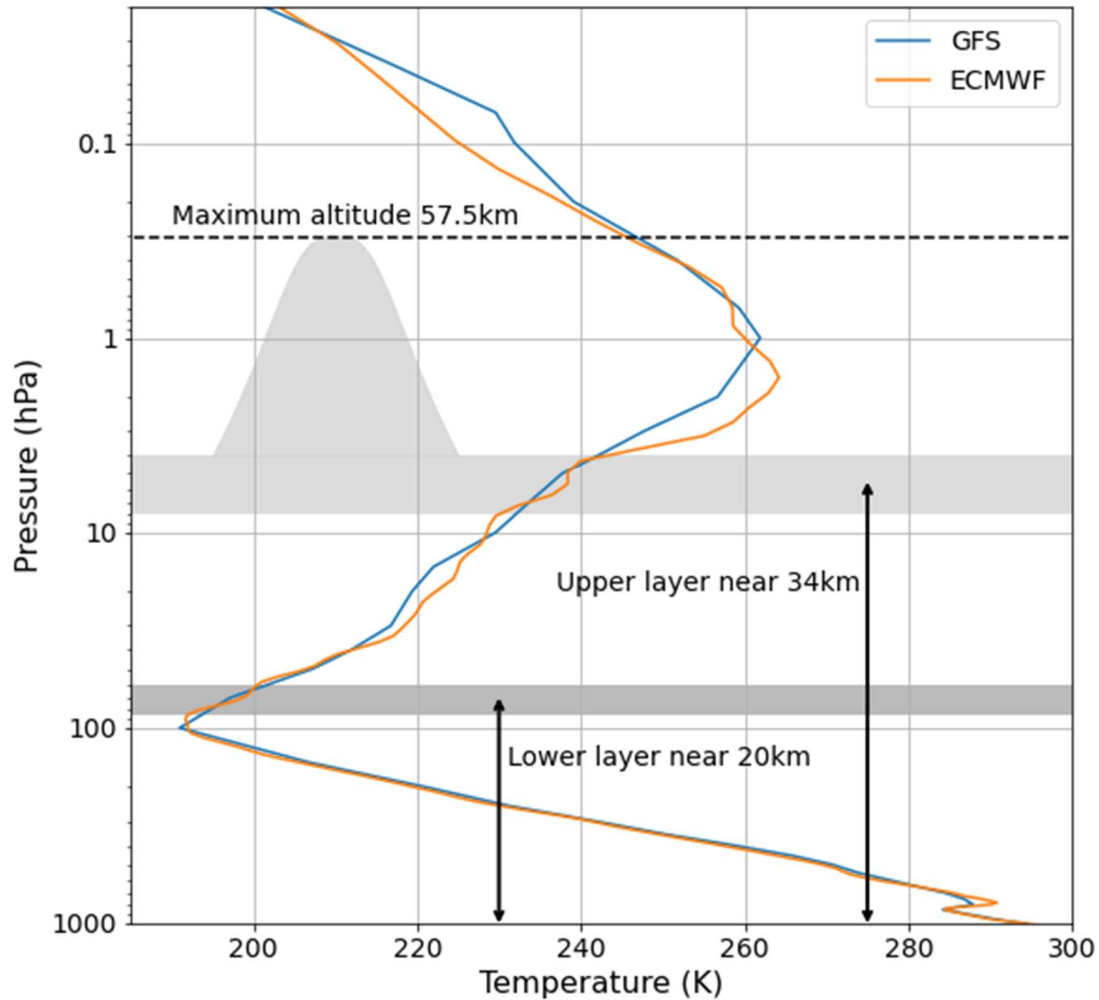
Fig 4. Vertical structure of the volcanic plume. A lower near-tropopause layer, whose altitude cannot be accurately determined, the main umbrella at higher altitude and the dome-like protrusion seen in the 04:30 UTC satellite images. Layer thickness is computed from the spread of parallax-based altitude retrievals for each layer and - when optically thick - the infrared brightness temperature approach. Overlaid are the 00:00 UTC GFS and ECMWF temperature profiles that show the tropopause near 100hPa and the stratopause at between 1-1.5hPa.

Science

AAAS

Supplementary Materials for

The January 2022 eruption of Hunga Tonga-Hunga Ha'apai volcano reached the mesosphere

Simon R Proud, Andrew Prata, Simeon Schmauß

Correspondence to: simon.proud@stfc.ac.uk

This PDF file includes:

Materials and Methods

Satellite data

In this study we use data from three geostationary satellites, GOES-17, Himawari-8 and GK-2A. Data was downloaded via the open APIs listed in the paper acknowledgements and processed using version 0.33.1 of the Satpy tool *(30)*. We converted the satellite data for each 10-minute timestep into both "true color" imagery that merges information from images taken at multiple wavelengths to mimic what the human eye would see and into single-wavelength images at the highest possible spatial resolution (band 3 for all satellites). These images were radiometrically calibrated from digital counts into radiance using the calibration coefficients supplied in the raw data files. We did not perform any atmospheric correction to these images, so they are affected by Rayleigh and aerosol scattering as well as gaseous absorption. This is not problematic for our study as we are not reliant upon the radiance values themselves, only upon feature matching between images. We consider that applying atmospheric correction would not add value, especially as the volcanic plume was at high altitude and hence, unlike clouds in the lower troposphere, relatively unaffected by scattering and absorption processes.

For the temperature-based estimates of plume altitude we generated temperature images for Himawari-8's channel 13, which is centered at 10.3 micron, and converted from digital number to brightness temperature using the default operator-supplied calibration, not the alternative GSICS calibration. Himawari-8 was chosen as it is located closest to the volcano and hence minimizes parallax-induced distortion and effects due to atmospheric absorption and scattering along the signal path length.

Selection of points for altitude calculation

Using the satellite imagery described in the previous section we manually identified a series of points within the plume that were readily identifiable across all three satellites. These were often prominent features such as cloud edges, bright spots – usually the tops of the highest clouds – and dark spots denoting troughs or shadows in the cloud tops. We also attempted automatic feature detection using a machine learning framework, but found that this performed poorly, most likely due to the significant intra-satellite image distortion introduced by the satellites viewing the plume from very different geometries meaning that shadows and highlights were often visible to one satellite but not the others. In addition to the tri-satellite feature matching, we also focused on the 04:30 UTC images from GK-2A and Himawari-8 to select a larger number of common points between these two satellites to map cloud topography. We excluded GOES-17 from this portion of the analysis as it viewed the plume from the opposite direction, which limited the number of high-quality matches that were possible. The tri- and dual-satellite feature positions and estimated altitudes are given in Tables S2 and S3 respectively.

Parallax based height estimation

To estimate the height of the volcanic plume at each manually selected feature we use well-established methods based on the parallax between observed and actual plume position. In the simplest model, the difference between these two positions is a function of only the angle at which the satellite views the plume and the altitude of the plume itself, meaning simple trigonometric identities can be used to find the actual position if the observed position is known, or vice versa. However, geostationary satellite images the field of view is very large, and the curvature of the Earth must also be considered. Furthermore, each satellite uses its own definition of the Earth's shape (polar and equatorial radii) when generating its imagery data. We therefore use a cartesian coordinate system to perform the parallax correction with a predefined plume altitude as follows:

1) Retrieve satellite longitude, latitude, and altitude from the raw data. Also retrieve the Earth model (WGS84 or GRS80) used by the satellite and the two Earth radii.
2) Convert satellite position and feature position into cartesian coordinates for the Earth model used by each satellite.
3) Determine the position along a line from observed position to satellite position at which the line's altitude is equal to the plume altitude. This is the parallax-corrected location of the plume.
4) Convert the parallax-corrected position from Cartesian coordinates to geographic coordinates.

This approach requires the plume altitude, which is unknown. But we do know the observed position from multiple satellites and can therefore iterate of a range of altitudes, computing the parallax-corrected position for each satellite. The true altitude of the plume will be that at which the difference between the parallax corrected locations found from each satellite is minimized.

However, the above assumes that the satellites perfectly observe plume location and that the manual point selection has no inaccuracies. There is an uncertainty due to the pixel spacing of the instrument – we cannot locate features with precision better than the pixel spacing, and other factors such as noise and instrument jitter also affect location accuracy. Furthermore, the eruption examined here was very energetic and evolved rapidly. Although all three satellites have very similar ten-minute scan patterns there are small differences in the time at which they

observed the eruption – on the order of seconds – and this also adds uncertainty to the position. These factors are unknown so cannot be explicitly quantified as an uncertainty on our height estimate. Instead, we apply random Gaussian noise with standard deviation of 0.018 degrees (approx. 1.5km) to each of our observed plume positions and repeat the iterative altitude estimation process 2e6 times. The variation in retrieved altitude from this repetitive process can give us an indication of the altitude uncertainty and these values are also given in tables S2 and S3. The tri-satellite analysis produces consistently lower variation (~0.6km) compared to the dual-satellite analysis at 04:30 (~2.2km), which in part is likely due to the selection of clearer matchup points in the tri-satellite analysis, thus minimizing input position uncertainty, and in part due to the inclusion of GOES-17 on the opposite side of the volcano and thus providing a much greater separation between the observed position seen by the satellites.

The code used in the height estimation process outputs multiple variables: The actual plume latitude and longitude averaged across all two million repetitions of the estimation process for each observation, the mean retrieved altitude, the mean distance between closest observations for each satellite and the standard deviations of heights and distances. The mean height, however, is not necessarily representative of the actual height, and therefore we also chose to output the height estimated by a subset of the 100 closest repetitions of the code. This threshold and approach were decided upon by comparison of estimated altitude and actual altitude (derived using the temperature method described below) for clouds visible in pre-eruption images. We output the average height estimated by these 100 closest points, the standard deviation in these heights and the average distance between intra-satellite parallax corrected position. For the figures and manuscript text we use the heights derived from the closest 100 points, but all output information is given in the supplementary tables.

Temperature based height estimation

In addition to the approaches described above, we also estimated plume height from the Himawari-8 temperature measurements made at 10.3μm. This band was chosen as it is a 'window' channel, does not overlap any strong absorption features and thereby provides an accurate temperature estimate of the object being observed. Most existing temperature-based height retrievals are designed to operate in the troposphere and therefore do not produce accurate results for such high plumes as generated by the Hunga-Tonga eruption. We therefore wrote our own very simple height retrieval that compares an observed cloud temperature to the temperature profile provided by the ECMWF operational analysis at 00z (approx. 4 hours prior to the eruption) and selects the altitude at which the ECMWF temperature is closest to the cloud temperature. Some portions of the plume in the stratosphere are significantly colder than the surrounding air (known as 'undercooling') and therefore do not correspond to any point on the ECMWF profile. For these points we assumed that they cool at a constant lapse rate of -6.5K/km relative to the tropopause temperature of 191.7K (at 90.9hPa, 17.3km altitude). This lapse rate assumption is based on our analysis of undercooling of overshooting tops from severe storms and may not be valid for this eruption but is the best estimate available.

To generate the statistics shown in figure 3 we extracted altitude estimates only for pixels associated with the plume itself. We did this by first masking out all pixels warmer than 250K, as very few plume pixels displayed such warm temperatures, and these were in the central – very high altitude – plume core where the ECMWF temperature profile is likely to be unrepresentative. The remaining pixels warmer than 250K were all associated with clear sky or

very low cloud unrelated to the eruption. Therefore, this temperature threshold enabled us to select only plume pixels and convective cloud pixels. Next, we used the *scipy* and *scikit-image* python libraries to erode the binary mask of pixel temperatures (removing speckle), fill small holes and then segment the resulting binary in labelled zones of low temperature pixels. Finally, we selected the labelled region that overlapped the location of the volcano and designated this as the volcanic plume. This approach failed for the first two timesteps (04:10 and 04:20 UTC) after the eruption due to insufficient development of the plume but was successful thereafter.

Stereoscopic vision height estimation
For the stereoscopic altitudes presented in Fig 3 we generated a digital elevation model (DEM) for each ten-minute timestep in the satellite data of the eruption from point clouds of the ash plume by using the commercial Agisoft Metashape software *(31)*. We used the high-resolution visible channel (at 0.6μm) for each of the three satellites. As Metashape is incompatible with the geostationary projection of the original data we resampled the Level-1 images onto a near-sided perspective projection with the same height and projection center as the original data. Subsequently, the images had to be georeferenced again in Metashape with the use of ground control points that we manually placed in each image on recognizable coastal features on the full disk images for each satellite. We assumed that the ground control points do not change between timesteps, which is a reasonable assumption given that satellite jitter and other factors have been corrected for in the original data.
The ground heights were approximated at zero meters above the GRS80 ellipsoid for simplification of the process, although this will introduce a small bias in the resulting altitudes. Initially this resulted in large projection errors as the near-sided perspective projection didn't account for the oblateness of the GRS80 ellipsoid, this could however be minimized by enabling the B1 (affinity) distortion correction in Metashape which flattened the images in the latitude axis to reintroduce the oblateness. The resulting alignment showed positional errors of ~2000m for markers in the Vicinity of Tonga. The final point cloud was calculated at 4 points per square kilometer and a DEM was generated at 1km resolution in equirectangular projection.
Lastly, we used the plume identification method described in the previous section to extract only those altitudes associated with the plume itself and we derived the altitude statistics shown in Fig 3 from these identifications.
This approach has considerable uncertainty compared to the manual identification of features used for the parallax correction method but allows analysis of the full plume rather than a subset of features. We compared the two methods and found that this stereoscopic approach produces altitudes up to 2.2km higher and 1.6km lower than the parallax method. Nevertheless, within these bounds the altitudes match well, and thus we have confidence in the timeseries of altitudes shown by this method being an accurate description of the trends in plume height.

Satellite name	GOES-17 *(32)*	Himawari-8 *(33)*	GK-2A *(34)*
Sensor name	ABI	AHI	AMI
Nominal longitude	137.2ºW	140.7ºE	128.2ºE
Scanning frequency	10 minutes*	10 minutes	10 minutes
0.455μm		1	
0.47μm	1		1
0.51μm		1	1
0.64μm	0.5	0.5	0.5
0.86μm	1	1	1
1.38μm	2		2
1.61μm	1	2	1
2.26μm	2		2
3.9μm	2	2	2
6.15μm	2		
6.25μm		2	2
7.0μm	2	2	2
7.4μm	2	2	2
8.5μm	2		
8.6μm		2	2
9.6μm		2	2
9.7μm	2		
10.3μm	2		
10.4μm	x	2	2
11.2μm	2	2	2
12.3μm	2	2	
12.4μm			2
13.3μm	2	2	2
*GOES-17 enabled a 1-minute 'rapid scan' mode at 07:05 UTC			

Table S1. Summary of the satellites used in this study. The satellite position listed is the nominal position, and some drift from this is both normal and expected. Our parallax calculations use the actual instantaneous position rather than the nominal position. The scanning frequency is identical for all three satellites, we did not use the 1-minute GOES-17 data as this introduces inconsistencies when comparing across sensors. The wavelengths given in the table represent the central wavelength and the values given for each wavelength row are the nominal pixel spacing at the subsatellite point. For the location of the Hunga-Tonga volcano, actual pixel spacing will be wider than this. Blank boxes represent wavelengths not available for a given instrument.